INL/JOU-24-80005-Revision-0

# Local chemical ordering of a neutron-irradiated CrFeMnNi compositionally complex alloy

March 2025

Nathan Curtis, Adrien Couet, Calvin Parkin, Haiming Wen, Kaustubh Krishna Bawane, Fei Teng, Tiankai Yao, Mukesh Bachhav, Sohail Shah

INL/JOU-24-80005-Revision-0

# Local chemical ordering of a neutron-irradiated CrFeMnNi compositionally complex alloy

**Nathan Curtis, Adrien Couet, Calvin Parkin, Haiming Wen, Kaustubh Krishna Bawane, Fei Teng, Tiankai Yao, Mukesh Bachhav, Sohail Shah**

**March 2025**

**Idaho National Laboratory**
**Idaho Falls, Idaho 83415**

**http://www.inl.gov**

**Prepared for the**
**U.S. Department of Energy**
**Under DOE Idaho Operations Office**
**Contract DE-AC07-05ID14517**

**Title:** Local chemical ordering of a neutron-irradiated CrFeMnNi compositionally complex alloy

**Author List:** Nathan Curtis[1], Sohail Shah[2], Mukesh Bachhav[2], Kaustubh Bawane[2], Fei Teng[2], Calvin Parkin[1], Tiankai Yao[2], Haiming Wen[3], Adrien Couet[1]

[1]University of Wisconsin – Madison

[2]Idaho National Laboratory

[3]Missouri University of Science and Technology

## Abstract

While ion-irradiation studies are a critical first step in studying compositionally complex alloys (CCAs) for nuclear applications, they do not capture all the microstructural changes occurring under the low irradiation dose rates and different particles' scattering patterns experienced in a nuclear reactor setting. To explore these phenomena in reactor-relevant conditions for the first time in CCA, the single-phase solid-solution $Cr_{10}Fe_{30}Mn_{30}Ni_{30}$ was neutron irradiated up to 6.61 displacements per atom at 395 and 579 °C. Irradiation-enhanced local chemical ordering (LCO) well beyond the range of short range ordering was observed, and is predicted to be the precursor to the precipitation of a coherent Ni-Mn $L1_0$ phase and a Cr-rich α' phase, though TEM analysis did not indicate the presence of either in any irradiation condition. The line density of faulted dislocation loops decreased from 6.47 to $1.69 \cdot 10^{15}$ $m^{-2}$ from 3.43 to 6.61 dpa at 579 °C despite no appreciable faulted loop content in the unirradiated material. LCO is expected to increase the complexity of the energy landscape within this alloy, restricting interstitial point defect mobility and creating local regions of greater stacking fault energy. These contribute to the negative correlation between irradiation dose and faulted dislocation loop density in this study, as well as the lack of void swelling observed.

## Graphical Abstract

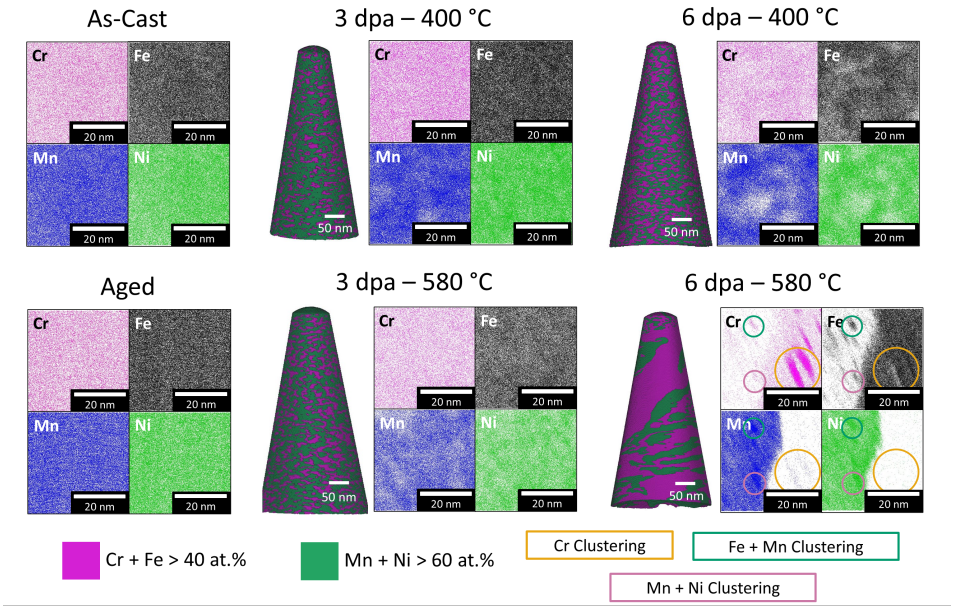

# 1 Introduction

As the nuclear energy community continues to innovate and propose more efficient and sustainable reactor designs, the limitations imposed by available materials become glaringly apparent. Current ASME code-certified structural materials are suitable for pressurized-water reactors and boiling-water reactors, yet their performance drastically suffers when exposed to the high temperatures and irradiation doses anticipated by future reactor concepts [1]. For instance, lead- and sodium-cooled fast reactors anticipate operational temperatures up to 600 °C and irradiation doses up to 150 displacements per atom (dpa), far more aggressive conditions than the 300 °C temperatures the current fleet experiences [2]. Next-generation molten salt-cooled and Very-High-Temperature reactors are following suit, posing challenges for both mechanical and corrosion performance when implementing currently certified materials [2,3]. To address these challenges, developing materials with enhanced irradiation tolerance is at the forefront of nuclear material design.

Over the lifetime of a nuclear reactor, the continued bombardment of neutrons from fission generates point defects within the microstructure. These, in turn, evolve into extended defects such as embrittling dislocation loops and empty cavities which compromise the structural performance of components and limit their operational lifetimes [4,5]. As irradiation temperatures increase for advanced reactor concepts, the point defects generated by irradiation have greater mobility to diffuse and coalesce into these larger extended defects [6,7]. This increase only occurs up to a certain point at which the high operational temperatures lead to thermal annealing of defects and void extended defect formation is less apparent in post-irradiation examination [8]. However, these high temperatures exceed 600 °C, at which creep resistance becomes a concern for many code-certified materials [1,8,9]. Several methods have been proposed to reduce irradiation damage accumulation within structural materials, and while recent efforts have included developing novel materials purpose-built for enhanced irradiation damage resistance, methods of microstructural tuning such as grain refinement and oxide-dispersion strengthening have historically dominated this field of research [10–13].

Compositionally Complex Alloys (CCAs), also referred to in literature as “High-Entropy Alloys”, are a class of novel research alloys unique due to their lack of a single principal element [14,15]. Instead of conventional alloying techniques to tune a base element’s performance, CCAs are composed of multiple elements in appreciable quantities such that their properties are derived from the interaction of each species with each other [16]. Retained strength at low temperatures, superior corrosion resistance, and high strength while retaining ductility are all properties previously exhibited by CCAs [17–22]. It should be noted, however, that these are not all present at the same time, and compromise must be made in compositional design for targeted applications like nuclear reactors [16].

The CCA property most intriguing for structural nuclear applications is a reportedly enhanced irradiation tolerance in comparison to current code-certified materials [23–25]. Several theories provide explanations for this irradiation resistance, chiefly driven by the complex energy landscape created by such a chemically diverse solid-solution crystal structure [23,26]. A hypothesis currently discussed in the community is that during the initial damage event where an incident neutron creates a cascade of atomic displacements from their lattice sites (i.e. thermal

spike), the energy imparted remains localized to the damage cascade longer than conventional alloys due to increased phonon scattering in CCAs [27–29]. The longer thermal spike lifetime would enhance the athermal recombination of point defects created during irradiation damage, reducing the overall impact of the initial damage event. Another hypothesis is that once defects have been created, their mobility navigating the complex lattice and energy landscape of CCAs is impeded [30], reducing their ability to cluster together for extended defect formation. CCAs also have displayed greater variety in point defect migration energies as a consequence of this complex energy landscape, with vacancy and interstitial migration energies even overlapping [30]. This overlap of migration energies would promote point defect recombination locally instead of point defect migration and agglomeration, further reducing the severity of extended defect formation [30,31]. Indeed, rather than generating large extended defects, a greater population of smaller voids and dislocation loops are seen forming under irradiation of CCAs [26,32,33]. The result are alloys which display higher density of smaller extended defects leading to overall lower hardening and void swelling, and greater apparent phase stability, suggesting enhanced irradiation tolerance and a potentially increased lifetime before irradiation-induced effects can cause failure in components.

The high-damage irradiation studies on CCAs to date, however, are primarily based on heavy-ion irradiations to achieve near end-of-life damage levels. While these ion irradiations are useful for studying extended defects formed at high irradiation doses, they are not without shortcomings. Due to the relatively high damage rate of heavy ions, the effect of ballistic mixing is more present within the irradiated region of samples which reduces the ability for processes such as thermal diffusion to occur in the irradiated region as they would in operation [16,34]. Notably, the superior phase stability exhibited by many ion irradiation studies has been shown to be a dose rate-dependent effect within CCAs too [34]. This makes heavy ion irradiation data difficult to apply for predicting CCA performance in nuclear reactor environments, where dose rate is much lower and time at elevated temperatures is greatly increased. Limited ion irradiation work on CCAs has also been performed at lower doses, for instance up to 7 dpa in-situ at Argonne National Lab's IVEM-Tandem facility, to study the evolution of irradiation response for the CrFeMnNi system, though the damage rate in that study is still orders of magnitude greater than the damage rate expected under neutron irradiation [32]. Complicating matters even further, the damage produced by ion irradiation is not constant throughout the damage region, with large damage gradients due to the interaction of charged particles in the material [31], and the results are quite difficult to translate to neutron irradiation damage. Unfortunately, neutron irradiation experiments are expensive due to the limited facilities available for both irradiation and post-irradiation examination, and the long irradiation times and cooldown after material activation greatly increase the time required for a full neutron irradiation study. As a result, the gold-standard of neutron irradiation experimentation is lacking for CCAs. What little data is available displays similar results to stainless steel alloys and show phase stability in a CrFeMnNi CCA, though this reported study only provides insight in neutron irradiation response near room temperature and to only 1 dpa [35].

In order to consider CCAs for future structural nuclear applications, it is vital to study their irradiation performance at reactor-relevant conditions. This work studies a series of $Cr_{10}Fe_{30}Mn_{30}Ni_{30}$ CCAs neutron-irradiated up to 6.6 dpa at 579 °C to provide a first look into the

evolution of neutron-irradiation response of CCAs at reactor-relevant temperatures.

# 2 Methods

## 2.1 Sample Fabrication

The alloy selected for irradiation in this project is nominally $Cr_{10}Fe_{30}Mn_{30}Ni_{30}$ and was chosen as a variation on the Co-free Cantor alloy previously studied for nuclear applications [21,35]. CALPHAD modelling guided the choice to reduce chromium content to only 10 at.%, far below an equimolar concentration, in an effort to preserve a single-phase face-centered cubic (FCC) microstructure at target operational temperatures for mechanical performance concerns. The single-phase nature of this alloy also allows for more direct analysis of CCA performance in terms of irradiation response of a compositionally complex matrix, as secondary phases require a more complex deconvolution of irradiation effects. This alloy was arc-melted in an Argon environment using Cr, Fe, Mn, and Ni with elemental purity all above 99.9 at.%., then homogenized for 10 hours at 1200 °C. The actual composition as measured by atom probe tomography (APT) is slightly iron-rich compared to nominal, and is listed in table 1. Samples were then polished to a final cleaning with a colloidal silica suspension with 0.02 µm particulate size for later sample preparation with a focused ion beam. To separate the in-reactor irradiation effects from purely thermal effects, since the neutron-irradiated samples spent up to 10,000 hours at temperature during irradiation, the as-fabricated material has been heat treated for 200 hours at 690 °C. The sample was encapsulated in quartz tube with titanium sponge as an oxygen getter, then evacuated and backfilled with argon 5 times to eliminate oxidation concerns during heat treatment. Since kinetic models are limited for CCAs, this temperature and exposure time aging conditions were selected based on atomic mobilities calculated by Computherm's Pandat® software (PanHEA database, 2023 version) to obtain similar atomic diffusion characteristic length for Mn, the least mobile of the elements in this composition, and thus reduce the aging time from 10,000 hours down to 200 hours while aging in the same FCC + BCC dual-phase stability prediction.

*Table 1. Measured composition (in atomic percentages) of the $Cr_{10}Fe_{30}Mn_{30}Ni_{30}$ material from APT.*

| Cr | Fe | Mn | Ni | Si | C | O |
|---|---|---|---|---|---|---|
| 9.74 ± 0.01 | 34.64 ± 0.01 | 28.26 ± 0.01 | 27.32 ± 0.01 | 0.04 | <0.01 | <0.01 |

## 2.2 Irradiation

The irradiation of this CCA was performed at Idaho National Laboratory's (INL) Advanced Test Reactor (ATR) as part of a Consolidated Innovative Nuclear Research (CINR) project on nanostructured materials for enhanced irradiation tolerance [36]. Irradiations occurred for up to 416 days for high-damage samples, and only 250 days for low-damage conditions at a rate of approximately $10^{-7}$ dpa/s. Simulations for flux and damage were performed using Monte-Carlo N-Particle modeling and overall damage was estimated using an atomic-weighted average displacement threshold energy and a time step-based accumulation of damage [37]. Both the targeted and calculated irradiation conditions are listed in table 2.

*Table 2. Summary of the four irradiation conditions present in this study. Targeted 2 dpa samples spent 250 days in Idaho National Lab's Advanced Test Reactor, while targeted 6dpa samples spent 416 days in-reactor.*

| | Irradiation Temperature (°C) | | Irradiation Damage (dpa) | | Time in |
|---|---|---|---|---|---|
| Sample Name | Target | Reported | Target | Reported | ATR (days) |
| 3 dpa – 400 °C | 300 | 368 | 2 | 3.09 | 250 |
| 3 dpa – 580 °C | 500 | 565 | 2 | 3.43 | 250 |
| 6 dpa – 400 °C | 300 | 395 | 6 | 6.52 | 416 |
| 6 dpa – 580 °C | 500 | 579 | 6 | 6.61 | 416 |

## 2.3 Focused Ion Beam

Sections of each irradiated sample were prepared for atom probe tomography (APT) and scanning transmission electron microscopy (S/TEM) using the FEI Quanta 3D FEG Focused Ion Beam at Idaho National Laboratory's Irradiated Materials Characterization Laboratory (IMCL). Both TEM lift-outs and APT tips were made near grain boundaries to study chemical segregation and defect evolution in both the bulk and intergranular region, though only TEM samples captured the grain boundaries in this study. TEM and APT samples were finished to thicknesses and base diameters of 100 nm, respectively, with a final milling at 5 kV, 50 pA of gallium before analysis. APT tips of the unirradiated material were also produced at INL, while TEM lift outs in the unirradiated material were performed at UW-Madison's Nanoscale Imaging and Analysis Center (NIAC) using a Zeiss Auriga gallium FIB with a final cleaning also at 5 kV, 50 pA.

## 2.4 Atom Probe Tomography

High resolution chemical analysis of each sample was collected with the IMCL's LEAP 5000XR Local Electrode Atom Probe (LEAP). All tips were run in pulsed laser mode, with a pulse energy of 40 pJ and frequency of 200 kHz at a maintained temperature of 55K and a constant data acquisition rate of 1%. 3D reconstructions and radial distribution functions (RDFs) were reconstructed using the Integrated Visualization and Analysis Software (IVAS) from CAMECA and analyzed inside of grains to quantify chemical segregation and local chemical ordering in the irradiated, aged, and as-fabricated materials.

## 2.5 Transmission Electron Microscopy

All TEM and STEM analysis of irradiated samples was performed with the FEI Titan Scanning TEM at Idaho National Laboratory's Irradiated Materials Characterization Lab (IMCL) at a 200 kV accelerating voltage, while unirradiated specimens were analyzed at the University of Wisconsin Madison's NIAC with a FEI Tecnai TF-30 TEM operating at 300 kV. STEM-EDS characterization of irradiated samples was collected to observe compositional changes in the bulk and grain boundary regions of each specimen. To investigate cavity formation within the bulk, high magnification STEM imaging was performed and contrast from over- and under-focused imaging was used to identify defects at high magnification [38]. Imaging of the faulted dislocation loops within the {1 1 1} planes was performed with darkfield imaging of the rel-rod present in the 1/3 (3  1) direction of the [1 1 0] zone axis, a technique which displays edge-on faulted dislocation loops [39,40].

# 3 Results

## 3.1 Unirradiated Material

TEM and X-ray diffraction (XRD) using the Bruker Discover D8 Diffractometer at UW-Madison's Nanoscale Imaging and Analysis Center (NIAC) confirmed a single-phase FCC solid solution with a lattice parameter of 3.618 ± 0.001 Å, and no visible faulted dislocation loops were observed during TEM analysis. The FCC matrix of the aged sample displayed a lattice parameter of 3.617 ± 0.002 Å and no discernable faulted dislocation loop content either. CALPHAD modeling using the Computherm's Pandat HEA database (PanHEA 2023) suggests the presence of a secondary Cr-rich BCC phase from 500 to 700 °C, replaced by ordered MnNi-rich Beta and CrFeMn Heusler $L2_1$ phases below 360 °C and 540 °C, respectively (Figure 1). It is worth noting that earlier version of the databases were only predicting a single phase FCC above 360 °C. APT of both the homogenized bulk and aged-unirradiated samples revealed no chemical segregation, with RDF data indicating chemical ordering on the length scale of a single unit cell.

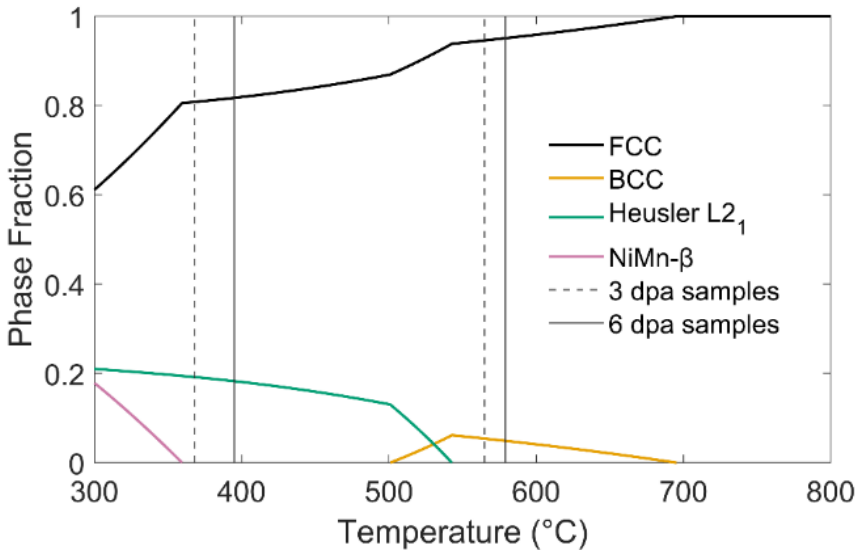


*Figure 1. The predicted phase composition of Cr10Fe30Mn30Ni30 from 300 to 800 °C and the temperatures at which each irradiation occurred*

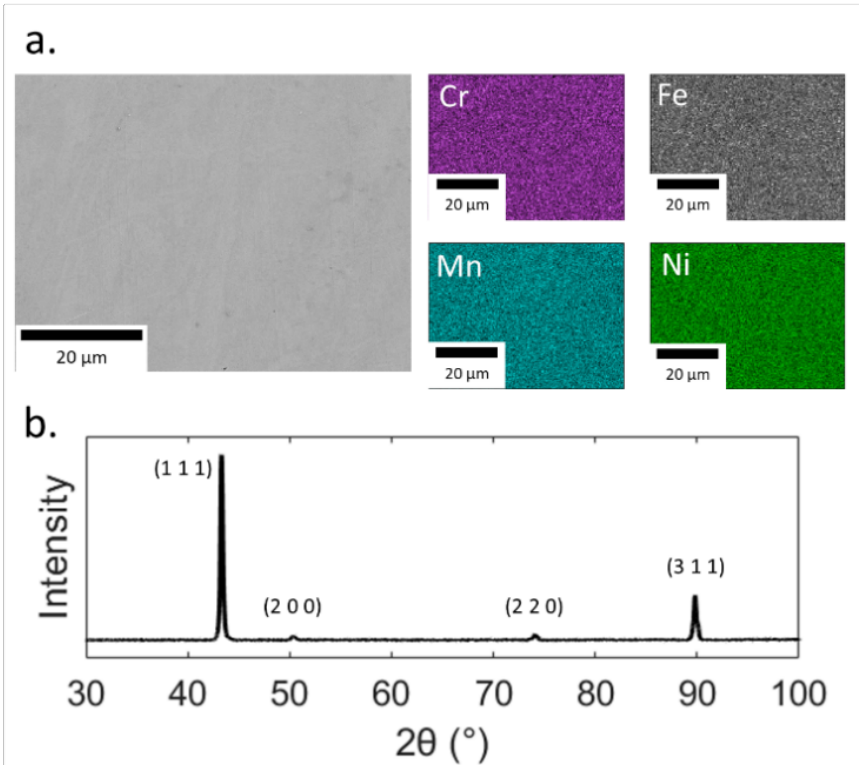


*Figure 2. a.) SEM-EDS intensity maps and XRD diffraction data from the a.) as-fabricated microstructure displaying chemical homogeneity, and b.) XRD diffraction data displaying a single-phase FCC lattice with a lattice parameter of 3.618 Å*

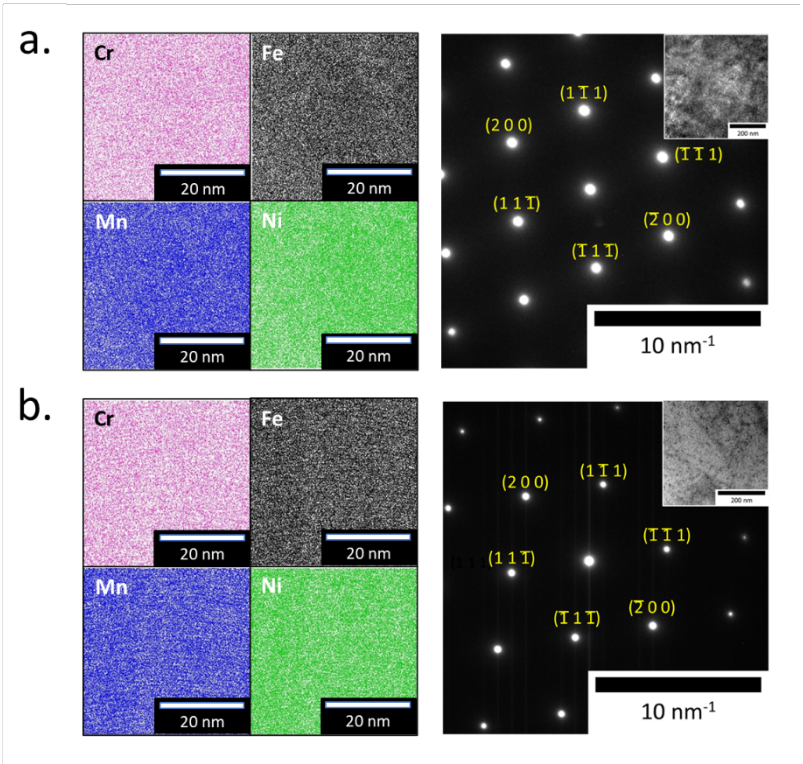


*Figure 3. 40 x 40 x 5 nm APT reconstruction slices and TEM diffraction data from the a.) as-fabricated and b.) thermally aged samples, both displaying solid solution with no chemical segregation and a lattice parameter of 3.618 Å*

## 3.2 Void Swelling

No clear voids were observed in any of the samples studied, though nano-scale imaging with over- and under-focused STEM imaging revealed contrasting features. The largest size of these contrast features was under 2 nm, and faceting (or lack thereof) was not resolvable to determine the nature of these defects; an example is available in the supplementary figures. Due to the small size and population of contrasting features present in the irradiated TEM foils, it is ambiguous whether they are helium bubbles stabilized in the matrix, voids, or experimental artefacts created during FIB preparation [41]. Comparing this to the work of Parkin et al., ion irradiation of single-phase CrFeMnNi CCAs to similar irradiation damage levels with the addition of helium has displayed cavity formation, though the total swelling from bubbles and voids only reached 0.3%, significantly less than the 1.4 and 5.8% swelling of the $Fe_{56}Ni_{44}$ binary alloy and pure Ni, respectively, in the same study [32]. It is inconclusive whether void swelling was present at any of the irradiation conditions for this study, and based on the results from Parkin et al., any potential void swelling is expected to be extremely small.

## 3.3 Faulted Dislocation Loops

Dislocation loop images and data are summarized in Figure 4 and Figure 5. Quantification of faulted loops in each sample reveals a decrease in dislocation loop size with increasing irradiation temperature. Samples 3dpa – 400 °C and 3dpa – 580 °C display faulted dislocation loops with average diameters of 14 and 7 nm, respectively, while their higher damage counterparts 6dpa – 400 °C and 6dpa – 580 °C have smaller dislocation loops on average (10 and 5 nm diameters). While there is overlap in these values including standard deviations, the sampled areas display an unexpected decrease in faulted loop densities with increasing damage for both irradiation temperatures. At 3dpa – 580 °C, a faulted loop density of $1.0 \cdot 10^{24}$ $m^{-3}$ is measured, while a density of only $3.3 \cdot 10^{23}$ $m^{-3}$ was present in the 6dpa-580 °C condition. A less pronounced effect is seen in the lower temperature condition, with a decrease from 4.7 to $3.6 \cdot 10^{23}$ $m^{-3}$ with increased irradiation damage.

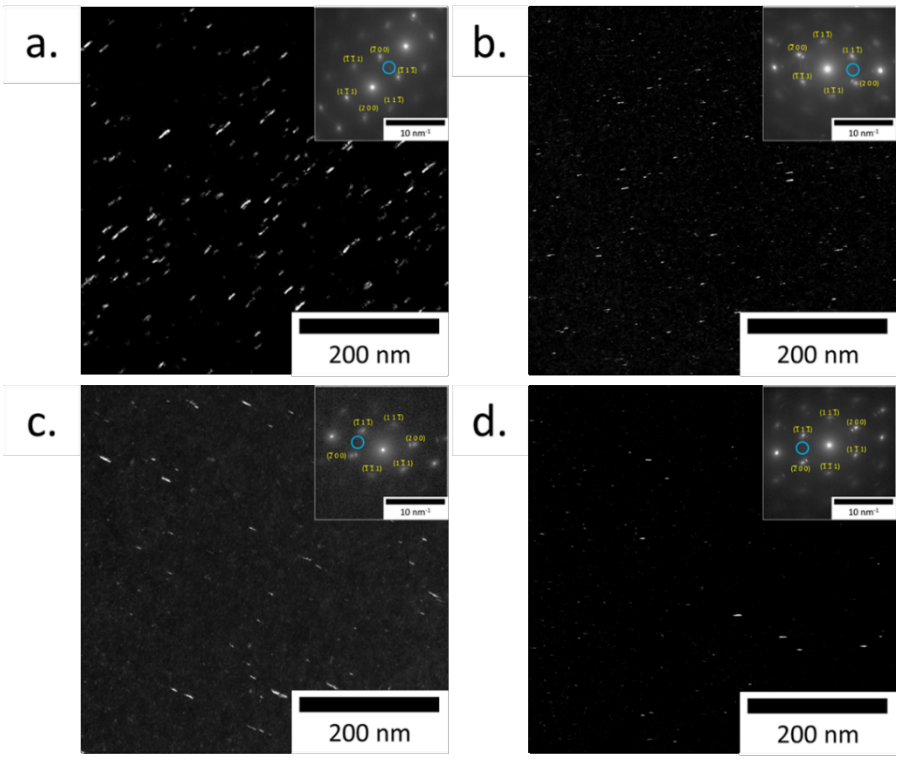


*Figure 4. Faulted dislocation loops from rel-rod contrast imaging from the {1 1 1} habit plane for a.) 3dpa – 400 °C, b.) 3dpa – 580 °C, c.) 6dpa – 400 °C, and d.) 6dpa – 580 °C*

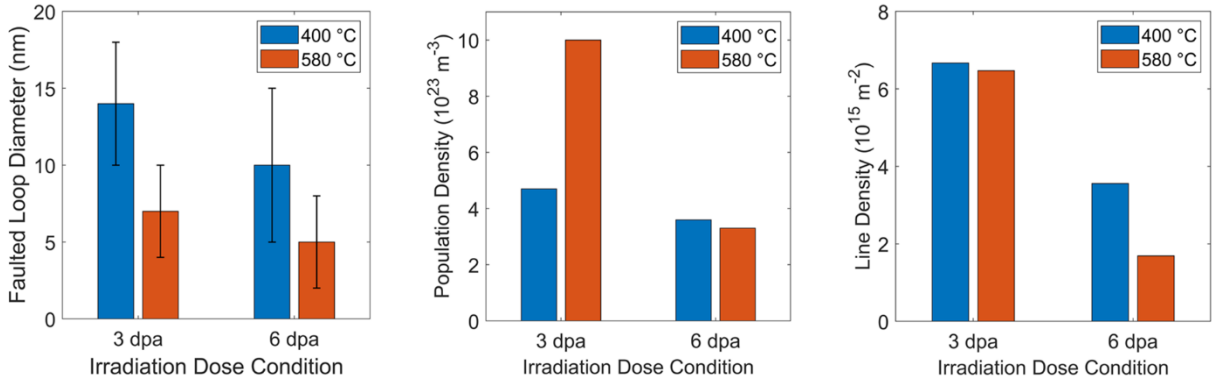


*Figure 5. Average faulted loop size (with standard deviation), population, and total line density from the {1 1 1} habit plane*

## 3.4 Lattice Distortion

The lattice parameter measured from the main diffraction pattern in the irradiated material was calculated to be 4.30 Å, though a coherent secondary diffraction pattern can be seen, displayed as small halos near the main diffraction pattern. Measurement of intensities in both the {1 1 1} and {2 0 0} directions suggest a second FCC structure with a lattice parameter of 3.68 Å (Figure 6). This distinct lattice mismatch present following irradiation suggests a decomposition into two distinct but coherent FCC phases, indicating either precipitate formation or chemical short-range ordering.

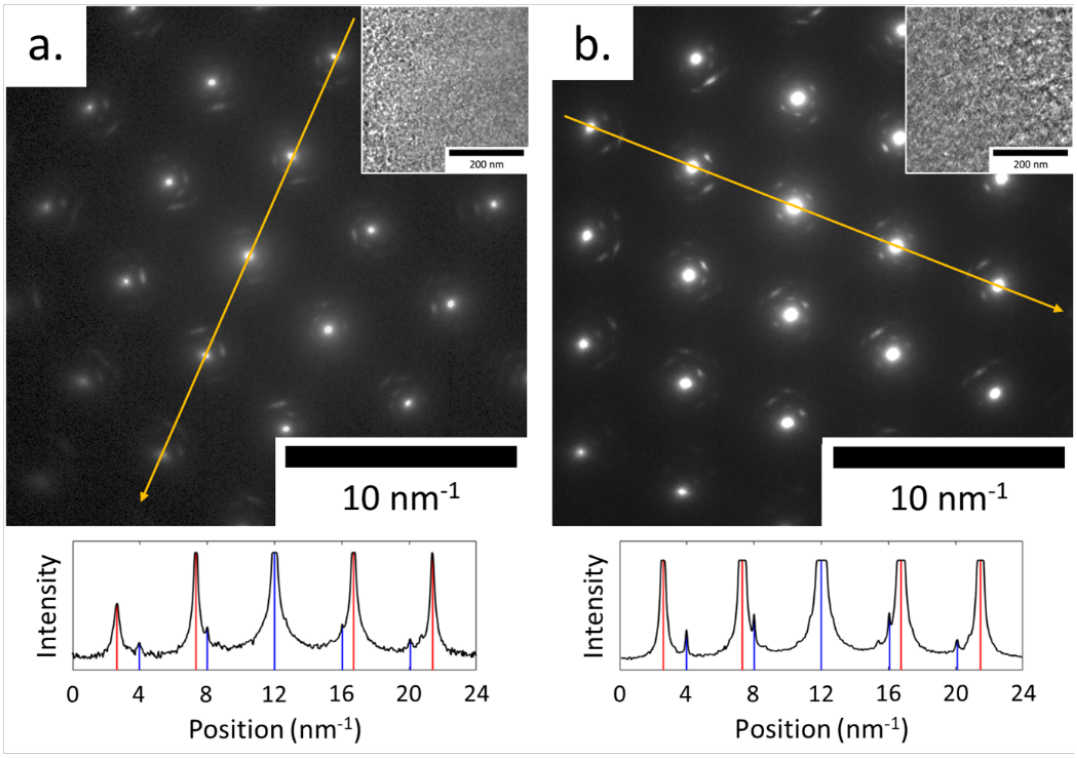


*Figure 6. [1 1 0] direction diffraction patterns and {1 1 1} line diffraction intensity of samples a.) 6dpa – 400 °C and b.) 6dpa – 580 °C. Each pattern displays two sets of diffraction spots corresponding to lattice parameters of 3.68 ± 0.03 and 4.30 ± 0.02 Å, respectively.*

## 3.5 Chemical Segregation

While most samples displayed no apparent grain boundary segregation from STEM-EDS measurements, a mild Ni enrichment by less than 5 at.% was observed at the grain boundary of the most aggressive irradiation condition (6dpa – 580 °C). The bulk of 3dpa – 580 °C, however, displayed an unexpected fine chemical segregation in a lamellar fashion within one of its grains. On the length scale of 7-8 nm, Cr and Fe preferentially segregate together, as do Mn and Ni. This is illustrated in Figure 8 with Fe and Mn, chosen for illustration purposes. The plot there shows the fluctuation of the composition relative to the initial bulk measurement. A positive value on this plot indicates an enrichment of Fe and lack of Mn, and the opposite for a negative value. This chemical fluctuation is constantly shifting along the segment seen in Figure 7, highlighting its banded nature in this sampleFigure 7. APT results, discussed below, provide the high resolution necessary to analyze this phenomenon further.

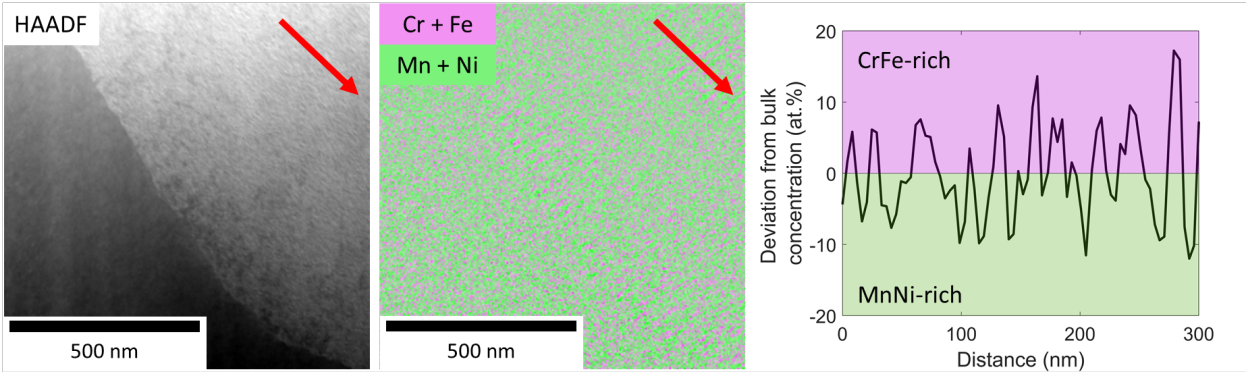


*Figure 7. Banded chemical segregation in the 3dpa – 580 °C sample, with a chemical variation plot to display the pairing of Fe and Mn in the sample.*

While little segregation is visible in the 3dpa – 400 °C APT sample, the scale of chemical segregation is visibly increased at both higher irradiation doses and temperatures (Figure 8). As a means of quantifying this ordering, radial distribution functions (RDFs) have been employed and summarized in Figure 9. Similar to the Warren-Cowley parameter which quantifies chemical short-range order (cSRO) [42], chemical RDFs parameterize the composition of a material relative to its distance from a chosen element with the following equation:

Where $r$ is the radial distance from element $i$, $x^{i\text{-}j}$ is the atomic fraction of element $j$ as a function of $r$, and $x_o^j$ is the bulk atomic fraction of element $j$. This is an imperfect system for quantifying segregation since it samples a spherical volume while the features of interest are notably non-spherical, it provides a tractable method of approximating the degree to which chemical ordering is occurring. In this instance LCO length will be defined by the RDF distance at which Cr-Fe and Mn-Ni co-segregation pairs reach their bulk concentration within the material as a function of their distance from Cr atoms (Figure 9).

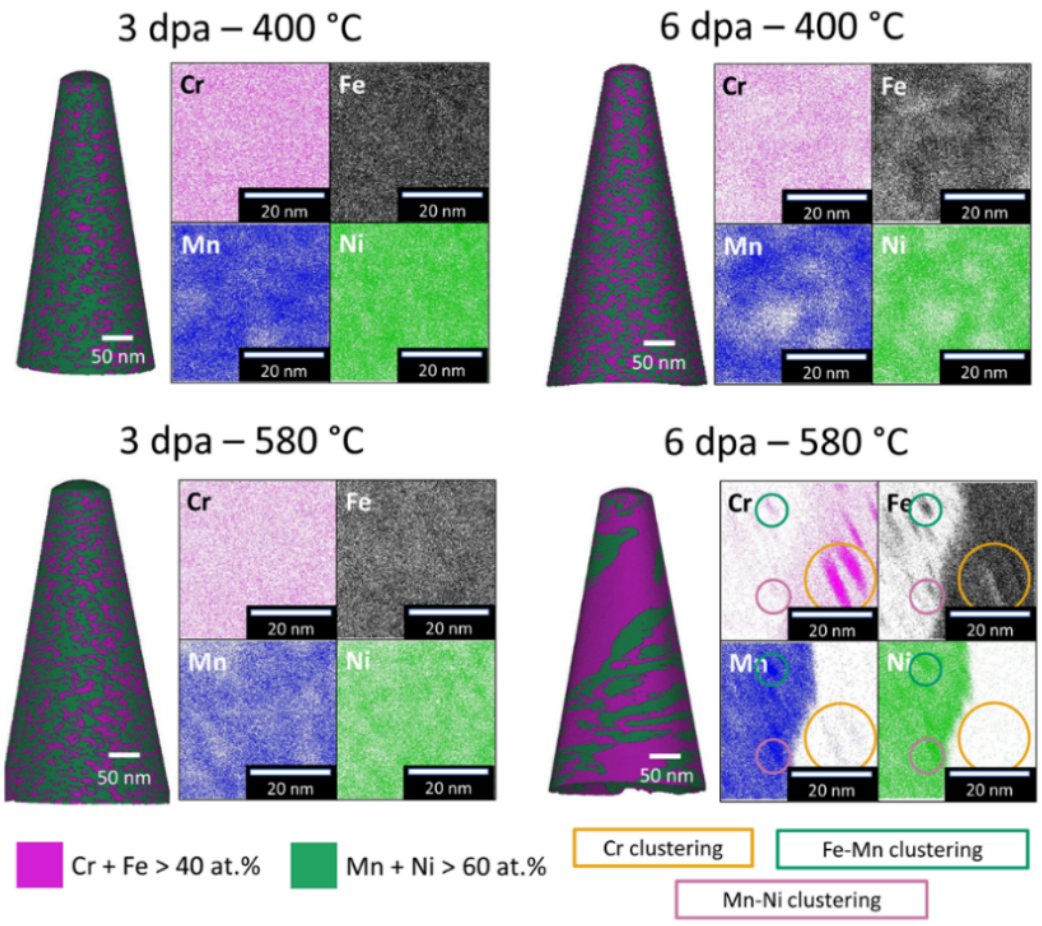


*Figure 8. APT isosurface maps displaying regions of Cr-Fe and Mn-Ni co-segregation enrichment from the bulk composition, and 40 x 40 x 5 nm slices from each tip. Regions of local clustering within the co-segregated regions have been identified in the 6 dpa 580 °C sample*

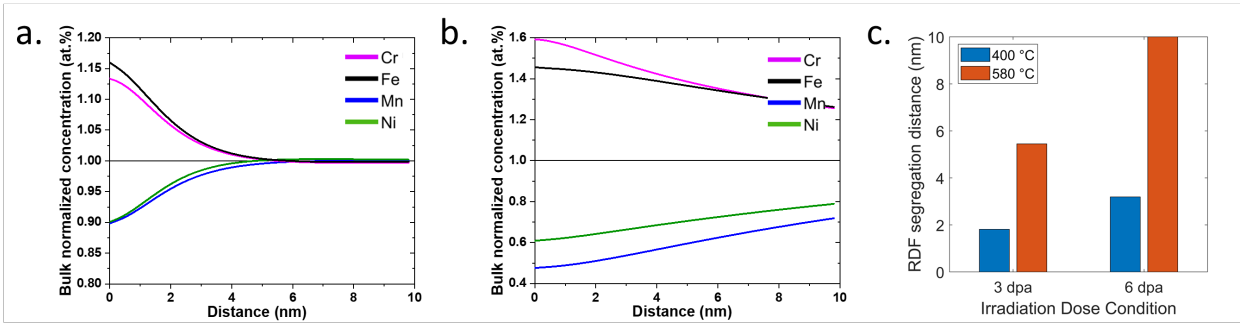


*Figure 9. The radial distribution functions for the 580 °C samples at a.) 3 and b.) 6 dpa, and c.) the chemical ordering distance based on RDFs centered around Cr atoms for all irradiated sample*

At 400 °C the ordering length of Cr-Fe and Mn-Ni pairs increases from 1.8 to 3.2 nm at 3.09 and 6.52 dpa, respectively, and the samples irradiated near 580 °C display even longer ordering lengths, up to 5.4 at 3.43 dpa, and well past the 10 nm observation window of the RDF at 6.61 dpa. By comparison, the as-cast, unirradiated material displays an ordering length of 0.3 nm –

approximately one unit cell for this microstructure. The unirradiated sample aged at 690 °C also displays a similarly low ordering distance of 0.4 nm. These results indicate that, even at similar diffusion characteristic lengths, irradiation induces chemical ordering, and there is an increase in chemical ordering distance with irradiation damage. Furthermore, at similar irradiation damage doses, a higher irradiation temperature results in longer ordering distances for this alloy. In addition to the general Cr-Fe and Mn-Ni co-segregation pairs, there are notable Cr-rich, Fe + Mn-rich, and Mn + Ni-rich regions apparent in the 6 dpa 580 °C sample, indicating the beginning of secondary phase formation (Figure 8).

# 4 Discussion

Despite no chemical ordering in the as-fabricated and aged sample, all irradiated conditions displayed LCO, with greater ordering distance observed at higher irradiation temperatures and damage. Studies on cSRO are quite prominent in literature and have shown that chemical ordering, even on a small scale, has a significant influence on the mechanical and thermodynamic properties of CCAs [43–46]. Since LCO plays a critical role in material performance, it will be the primary irradiation effect of interest discussed in this study. On the other hand, no void swelling was observed in any of the neutron-irradiated CCAs. Faulted dislocation loop concentration, measured with rel-rod contrast imaging, decreased with both increasing irradiation temperature and damage. It should be noted that discussing the irradiation response in this study requires consideration of ion irradiations due to the lack of neutron irradiation data available for CCAs. To address potential inaccuracies expected from dose-rate dependent effects, studies discussed in this section are supplemented by molecular dynamics (MD)-based simulations or directly discuss the influence of dose rate, when available.

Research of cSRO's influence on extended defect accumulation under irradiation is limited, though coupled atomistic modelling and ion irradiation studies provide some insight on the phenomena occurring in these conditions. In Zhang et al.'s research of a CrCoNi CCA, a 32% reduction in irradiation-induced defect density was observed after ion irradiation in LCO samples when compared to the random solid solution [47]. MD modelling of the point defect formation energy in this study showed little difference between the random solid-solution and chemically-ordered CrCoNi. As a result, the cascade-induced point defect concentration was influenced minimally by LCO's presence during the initial damage event. Kinetically, however, the activation energy for both interstitial and vacancy migration was calculated to be greater with LCO, and a greater energy penalty for defect mobility was seen for interstitials over vacancies [47]. This is especially relevant since interstitials typically have much greater mobility and are expected to annihilate at defect sinks such as grain boundaries before vacancies can diffuse. By reducing the rate at which they will annihilate, a greater interstitial population is available for recombination with vacancies in the bulk to reduce the surviving irradiation-induced point defect density over time, and thus reduce the extended defect density [31]. Another feature of LCO seen in MD-MC studies is a greater trapping of dislocations and defect clusters due to LCO's tendency to further increase the complexity of the energy landscape in CCAs [48–52]. The restricted mobility of interstitial clusters has been proposed as a means of reducing void formation by again increasing the availability of interstitial point defects available for recombination with the slower-diffusing vacancies [48]. The impeded mobility of both interstitial point defects and clusters enhances recombination with vacancies to reduce void swelling, a

finding consistent with many experimental- and modelling-based CCA ion irradiation studies [21,23,26–29,32,47,48].

While FIB damage during preparation of TEM samples prevented studying the full dislocation network, reported neutron-irradiation studies on metallic materials generally display an increase in dislocation line density with increased irradiation damage [53,54], and this discussion will assume similar behavior for these neutron-irradiated CCAs. The faulted dislocation loops observed experimentally decreased in size, line density, and population with increasing irradiation dose and temperature, which could have several causes.

One theory from Parkin et al. suggests that materials with greater stacking fault energy (SFE) will have a reduced faulted loop nucleation rate and maintain fewer faulted loops since higher stacking fault energy increases the barrier for interstitial cluster collapse and formation of stacking faults [30]. The enhanced loop unfaulting is based on the concept of a critical stacking fault energy that, when surpassed, makes prismatic loops more energetically favorable which promotes loop unfaulting [56]. Greater SFE would decrease the critical size of these faulted loops, which would be reflected experimentally by a decrease in the average faulted dislocation loop size observed. The tendency for loops to unfault more readily in the CrFeMnNi system from their study was attributed to Mn content exceeding 15 at.%, which has been experimentally shown to increase SFE in the matrix [32,55]. The alloy studied here is already be expected to have high SFE due to its nearly 30 at.% Mn in the bulk, and locally is expected to have even greater SFE due to local enrichment with LCO. This would increase the regions of high SFE within the matrix and decrease the critical faulted loop size further, albeit locally. This offers one explanation for the decreased faulted loop size and population observed with both increasing irradiation dose and temperature in this study.

This SFE-based theory conflicts with the later work of Daramola et al., however, whose MD simulations found that an austenitic stainless steel is expected to experience greater loop unfaulting than a CrFeMnNi CCA, despite having lower SFE [57]. Their work primarily attributed the unfaulting of loops to the formation of Shockley partials, which would remove the stacking fault from loops and leave prismatic loops where faulted once existed [57]. Daramola et al.'s study proposed that Shockley partial formation and movement were more sensitive to SFE *fluctuation* instead of overall SFE, which would hinder movement due to greater lattice friction and reduce loop unfaulting [57]. SFE is expected to fluctuate significantly more in CCAs [30], which explains the decreased unfaulting in Daramola et al.'s CCA over stainless steel. One key feature found in their study was that the lattice friction hindering Shockley partial movement is reduced at higher temperatures, which led to a corresponding relative increase in loop unfaulting within their CCA simulations [57]. While this justifies the lower population of faulted loops with increasing temperature, it does not explain the smaller loop size observed, especially with increased LCO at higher temperatures and doses.

One leading theory which may explain this is based on the interaction between faulted loops and other loop and line dislocations. MD simulations display that these interactions cause loop unfaulting or integration into the general dislocation network [58,59], and the work of Chen et al. found that it occurs more frequently as loops grow larger and have a higher probability of interacting [53]. Given that loops are expected to grow larger with increasing irradiation dose

and temperature [31], the larger faulted loops would more readily interact, unfault, and leave only a population of smaller faulted loops observable. This aligns with the results of this study, though it is imperative to note this is only a speculative explanation due to the lack of prismatic loop and dislocation network data in this study. While the mechanisms for this reduced faulted loop content are uncertain, it's clear the reduced faulted loop content is valuable for structural applications, as it has been shown to suppress irradiation-induced hardening rates in both CCAs and stainless steels [53,57,60]. The observed decrease in faulted dislocation loop content as a function of irradiation over time in this experiment may result in less severe irradiation-induced hardening, although this effect was not measured in our study.

While Cr-Fe and Mn-Ni co-segregation pairs are observed in this experiment, there is further chemical segregation occurring within these two regions. Cr-rich regions are observed within the Cr-Fe segregated region, though a distinct BCC precipitate, as predicted by CALPHAD, was not observed. While thermodynamics suggest an equilibrium between this Cr-rich BCC phase and a near-nominal composition FCC phase, this does not account for kinetics, which are expected to be sluggish in CCAs and would hinder its formation [26]. Additionally, the Mn-Ni region of the 6 dpa – 580 °C sample contains both Mn-Ni and Fe-Mn enriched regions. The Fe-Mn rich clustering is chemically similar to that of the predicted $L2_1$ phase, but again no BCC-structured phase has been identified in this alloy under TEM. The Mn-Ni rich regions in this work are consistent with alloys which share similar predicted phase compositions, such as $Cr_{18}Fe_{29}Ni_{30}Mn_{23}$ and $Cr_{0.6}FeNiMn$ [34,61]. In these alloys from the works from Kamboj et al., heavy-ion irradiation at 500 °C up to 10 dpa resulted in the formation of NiMn-rich precipitates with an $L1_0$ microstructure [34]. Furthermore, when the dose rate decreased from $10^{-4}$ to $10^{-5}$ dpa/s up to 2 dpa, the size of Ni-Mn rich precipitates increased slightly, and their relative volume fraction nearly tripled, reaching 26% of the matrix [34]. In our study, while 420 days under irradiation at 579 °C up to 6.61 dpa displayed ordering of Ni-Mn segregation above 70 at.% NiMn within a radius of 3.4 nm throughout the APT tip, no superlattice spots for the $L1_0$ microstructure were observed under diffraction, and neither lattice parameter found in the two coherent lattices from diffraction matches the expected lattice parameters of 3.74 or 3.52 Å for NiMn $L1_0$ [62,63]. Thermal aging of the unirradiated specimen also revealed a lattice parameter of 3.617 Å and no coherent second diffraction pattern, which indicates that the LCO seen in the 580 °C (and likely also 400 °C) irradiations is indeed enhanced by irradiation. Finally, despite local enrichment of Cr and Fe in the matrix, there was no α′ phase observed. However, the nucleation of α' phase cannot be ruled out since the Cr-clustering observed in the 6 dpa 580 °C sample reached as much as 80 at.% concentration of Cr. Thus α' phase precipitation may be possible with longer exposure. This precipitation would be concerning for future application due to α′-driven embrittlement as observed in FeCrAl alloys [64–66]. While no actual precipitate formation was observed in this work, the chemical segregation observed is expected to be the precursor to eventual Ni-Mn-rich $L1_0$, Cr-rich α', and Fe-Mn-rich $L2_1$ precipitations. The formation of coherent precipitates and α' would likely inhibit dislocation motion, increasing overall strength and potential embrittlement [64,67].

LCO does not only impact the irradiation response of CCAs, it directly impacts their mechanical performance too. The presumed increase in stacking fault energy present in this study, caused by the tortuous energy landscape observed in solid solution CCAs and further roughened by Mn-rich LCO regions, will increase the strength of this CCA by providing a larger energy barrier for

dislocation motion [46,68–70]. While this may increase strength, the presence of LCO in CCAs has been observed to generate wavy dislocations, indicating both dislocation glide and climb are occurring [45,71]. MD simulations of the CrCoNi CCA from Li et al. propose that the "ruggedness" of the energy landscape with LCO guides the motion of dislocation climb and glide and creates select pathways for dislocations to move [45]. By restricting the available paths for dislocation motion their potential to interact is expected to increase, leading to greater work hardening through dislocation interaction and multiplication [71]. This increased work hardening has been seen in both experimental and modelling studies [46,51,67,69,72]. While the unfaulting of faulted dislocation loops may reduce the potential irradiation-induced hardening, prismatic loop and line dislocation motion are still impeded significantly by LCO. This, along with potential secondary phase precipitation, will significantly contribute to irradiation-induced hardening. It is expected, then, that an overall irradiation-induced hardening effect will be observed, but potentially delayed by early dislocation loop unfaulting enhanced by local chemical ordering. Future work including neutron-irradiated CCA tensile specimen is necessary to further expand on the effects of LCO and faulted loops on mechanical response.

# 5 Conclusions

In this work, the neutron irradiation response of a CCA was for the first time studied at operationally relevant temperatures. The $Cr_{10}Fe_{30}Mn_{30}Ni_{30}$ CCA was studied at 400 and 580 °C up to 6.61 displacements per atom. While no appreciable chemical ordering was observed in the as-cast and aged samples, irradiation-enhanced diffusion led to local chemical ordering far in excess of 10 nm. This is presumed to be the initial stages of a MnNi-rich $L1_0$, Cr-rich α', and potential FeMn-rich $L2_1$ phase precipitations. At this stage of irradiation, local chemical ordering further increases the complexity of the energy landscape within this CCA, which significantly impacts its irradiation response. The lack of apparent void swelling is attributed to increased activation energy for interstitial diffusion, one expected result of the LCO-roughened energy landscape. Reduced interstitial mobility facilitates greater point defect recombination after the initial damage cascade, limiting vacancy supersaturation necessary for void formation. Additionally, the high SFE expected from 30 at.% Mn content in the alloy is expected to increase the likelihood of dislocation loops unfaulting into prismatic loops at higher temperatures and doses, which would explain the decreased faulted loop concentration at higher irradiation doses.

# 6 Acknowledgements

Special thanks to Alina Montrose for scheduling and sample handling logistics, and the support staff at Idaho National Laboratory's Irradiated Materials Characterization Laboratory without whom this research would not be possible.

Special thanks to Andrew Hoffman and Michael Moorehead, whose guidance and mentorship have been instrumental in my development as a researcher and led to the work presented herein.

This material is based upon work supported under an University Nuclear Leadership Program Graduate Fellowship.

This work was supported by the U.S. Department of Energy, Office of Nuclear Energy under DOE Idaho Operations Office Contract DE-AC07-05ID14517 as part of Nuclear Science User Facilities award #22-4459.

Materials or samples employed in this study are from the Nuclear Fuels and Materials Library and were provided by the U.S. Department of Energy, Office of Nuclear Energy under DOE Idaho Operations Office Contract DE-AC07-051D14517 as part of the Nuclear Science User Facilities.

The authors gratefully acknowledge use of facilities and instrumentation in the UW-Madison Wisconsin Center for Nanoscale Technology. The Center (wcnt.wisc.edu) is partially supported by the Wisconsin Materials Research Science and Engineering Center (NSF DMR-2309000) and the University of Wisconsin-Madison.

### 6.1 Author Contributions

**Nathan Curtis:** Formal Analysis, Investigation, Visualization, Writing – Original Draft **Sohail Shah:** Formal Analysis, Visualization, Writing – Review and Editing **Mukesh Bachhav:** Formal Analysis, Investigation, Visualization, Writing – Review and Editing **Kaustubh Bawane:** Investigation **Fei Teng:** Investigation **Calvin Parkin:** Conceptualization, Funding Acquisition, Writing – Review and Editing **Tiankai Yao:** Methodology, Project Administration, Supervision **Haiming Wen:** Resources, Supervision **Adrien Couet:** Supervision, Writing – Review and Editing

## 7 Supplementary Figures

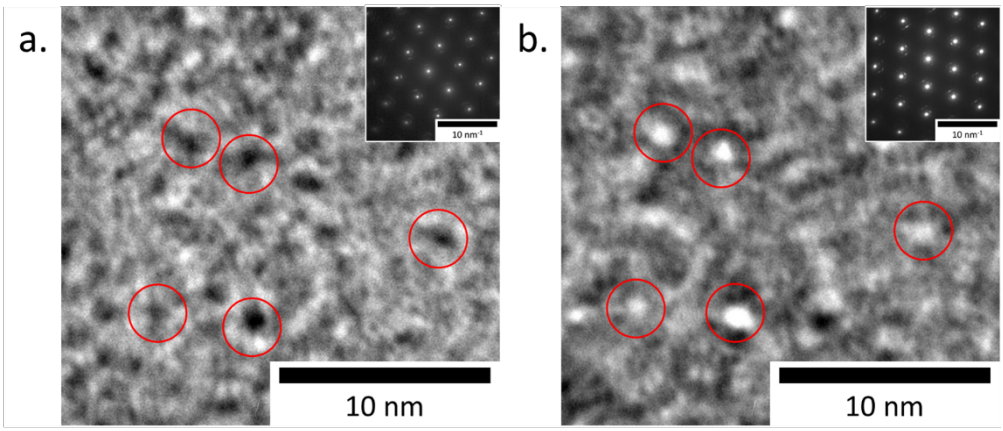


*Additional Figure 1. TEM images of potential cavities present using 500 nm of a.) overfocusing and b.) underfocusing. Potential cavities and bubbles have been circled for ease of viewing*

## 8 References

[1] R.N. Wright, Updated Draft ASME Boiler and Pressure Vessel Code Case for Use of Alloy 617 for Construction of Nuclear Components for Section III Division 5, (2018). https://doi.org/10.2172/1471711.

[2] S.J. Zinkle, J.T. Busby, Structural materials for fission & fusion energy, Materials Today 12 (2009) 12–19. https://doi.org/10.1016/S1369-7021(09)70294-9.

[3] J. Serp, M. Allibert, O. Beneš, S. Delpech, O. Feynberg, V. Ghetta, D. Heuer, D. Holcomb, V. Ignatiev, J.L. Kloosterman, L. Luzzi, E. Merle-Lucotte, J. Uhlíř, R. Yoshioka, D. Zhimin, The

molten salt reactor (MSR) in generation IV: Overview and perspectives, Progress in Nuclear Energy 77 (2014) 308–319. https://doi.org/10.1016/J.PNUCENE.2014.02.014.

[4] E. Zarkadoula, R.E. Stoller, Primary Radiation Damage Formation in Solids, Elsevier,New York,New York,United States of America, United States, 2020. https://www.osti.gov/biblio/1616821.

[5] W. Schilling, Properties of Frenkel defects, Journal of Nuclear Materials 216 (1994) 45–48. https://doi.org/https://doi.org/10.1016/0022-3115(94)90005-1.

[6] A. Hussain, R.S. Dhaka, H.J. Ryu, S.K. Sharma, P.K. Kulriya, A critical review on temperature dependent irradiation response of high entropy alloys, J Alloys Compd 948 (2023) 169624. https://doi.org/10.1016/J.JALLCOM.2023.169624.

[7] T. ni Yang, C. Lu, G. Velisa, K. Jin, P. Xiu, Y. Zhang, H. Bei, L. Wang, Influence of irradiation temperature on void swelling in NiCoFeCrMn and NiCoFeCrPd, Scr Mater 158 (2019) 57–61. https://doi.org/10.1016/J.SCRIPTAMAT.2018.08.021.

[8] W.G. Johnston, J.H. Rosolowski, A.M. Turkalo, T. Lauritzen, The depth distribution of void swelling produced by 5 MeV Ni ions, Journal of Nuclear Materials 62 (1976) 167–180. https://doi.org/10.1016/0022-3115(76)90014-3.

[9] M. Griffiths, Microstructural Effects on Irradiation Creep of Reactor Core Materials, Materials 16 (2023) 2287. https://doi.org/10.3390/MA16062287/S1.

[10] G.M. Cheng, W.Z. Xu, Y.Q. Wang, A. Misra, Y.T. Zhu, Grain size effect on radiation tolerance of nanocrystalline Mo, Scr Mater 123 (2016) 90–94. https://doi.org/10.1016/J.SCRIPTAMAT.2016.06.007.

[11] C. Lu, Z. Lu, X. Wang, R. Xie, Z. Li, M. Higgins, C. Liu, F. Gao, L. Wang, Enhanced Radiation-tolerant Oxide Dispersion Strengthened Steel and its Microstructure Evolution under Helium-implantation and Heavy-ion Irradiation, Scientific Reports 2017 7:1 7 (2017) 1–7. https://doi.org/10.1038/srep40343.

[12] A. Hoffman, M. Arivu, H. Wen, L. He, K. Sridharan, X. Wang, W. Xiong, X. Liu, L. He, Y. Wu, Enhanced Resistance to Irradiation Induced Ferritic Transformation in Nanostructured Austenitic Steels, Materialia (Oxf) 13 (2020) 100806. https://doi.org/10.1016/J.MTLA.2020.100806.

[13] X. Yan, Z. Su, J. Liang, T. Shi, B. Sun, P. Lei, D. Yun, T. Shen, G. Ran, C. Lu, Highly stable nanocrystalline oxide dispersion strengthened alloys with outstanding helium bubble suppression, Journal of Nuclear Materials 557 (2021) 153283. https://doi.org/10.1016/J.JNUCMAT.2021.153283.

[14] J.-W. Yeh, S.-K. Chen, S.-J. Lin, J.-Y. Gan, T.-S. Chin, T.-T. Shun, C.-H. Tsau, S.-Y. Chang, Nanostructured High-Entropy Alloys with Multiple Principal Elements: Novel Alloy Design Concepts and Outcomes, Adv Eng Mater 6 (2004) 299–303. https://doi.org/10.1002/adem.200300567.

[15] B. Cantor, I.T.H. Chang, P. Knight, A.J.B. Vincent, Microstructural development in equiatomic multicomponent alloys, Materials Science and Engineering: A 375–377 (2004) 213–218.

https://doi.org/10.1016/j.msea.2003.10.257.

[16] E.J. Pickering, A.W. Carruthers, P.J. Barron, S.C. Middleburgh, D.E.J. Armstrong, A.S. Gandy, High-Entropy Alloys for Advanced Nuclear Applications, Entropy (Basel) 23 (2021) 1–28. https://doi.org/10.3390/E23010098.

[17] O.N. Senkov, G.B. Wilks, J.M. Scott, D.B. Miracle, Mechanical properties of Nb25Mo25Ta25W25 and V20Nb20Mo20Ta20W20 refractory high entropy alloys, Intermetallics (Barking) 19 (2011) 698–706. https://doi.org/10.1016/j.intermet.2011.01.004.

[18] B. Gludovatz, A. Hohenwarter, D. Catoor, E.H. Chang, E.P. George, R.O. Ritchie, A fracture-resistant high-entropy alloy for cryogenic applications, Science (1979) 345 (2014) 1153–1158. https://doi.org/10.1126/science.1254581.

[19] A. V Kuznetsov, D.G. Shaysultanov, N.D. Stepanov, G.A. Salishchev, O.N. Senkov, Tensile properties of an AlCrCuNiFeCo high-entropy alloy in as-cast and wrought conditions, Materials Science and Engineering: A 533 (2012) 107–118. https://doi.org/10.1016/j.msea.2011.11.045.

[20] J. Zhu, S. Lu, Y. Jin, L. Xu, X. Xu, C. Yin, Y. Jia, High-Temperature Oxidation Behaviours of AlCoCrFeNi High-Entropy Alloy at 1073–1273 K, Oxidation of Metals 94 (2020) 265–281. https://doi.org/10.1007/S11085-020-09991-6.

[21] N.A.P.K. Kumar, C. Li, K.J. Leonard, H. Bei, S.J. Zinkle, Microstructural stability and mechanical behavior of FeNiMnCr high entropy alloy under ion irradiation, Acta Mater 113 (2016) 230–244. https://doi.org/10.1016/j.actamat.2016.05.007.

[22] P. Jinhong, P. Ye, Z. Hui, Z. Lu, Microstructure and properties of AlCrFeCuNix (0.6x1.4) high-entropy alloys, Materials Science and Engineering: A 534 (2012) 228–233. https://doi.org/10.1016/j.msea.2011.11.063.

[23] F. Granberg, K. Nordlund, M.W. Ullah, K. Jin, C. Lu, H. Bei, L.M. Wang, F. Djurabekova, W.J. Weber, Y. Zhang, Mechanism of Radiation Damage Reduction in Equiatomic Multicomponent Single Phase Alloys, Phys Rev Lett 116 (2016) 135504. https://doi.org/10.1103/PHYSREVLETT.116.135504/FIGURES/4/MEDIUM.

[24] T. Yang, C. Li, S.J. Zinkle, S. Zhao, H. Bei, Y. Zhang, Irradiation responses and defect behavior of single-phase concentrated solid solution alloys, J Mater Res 33 (2018) 3077–3091. https://doi.org/10.1557/JMR.2018.285/FIGURES/9.

[25] C. Lu, L. Niu, N. Chen, K. Jin, T. Yang, P. Xiu, Y. Zhang, F. Gao, H. Bei, S. Shi, M.R. He, I.M. Robertson, W.J. Weber, L. Wang, Enhancing radiation tolerance by controlling defect mobility and migration pathways in multicomponent single-phase alloys, Nature Communications 2016 7:1 7 (2016) 1–8. https://doi.org/10.1038/ncomms13564.

[26] Q. He, Y. Yang, On lattice distortion in high entropy alloys, Front Mater 5 (2018) 384340. https://doi.org/10.3389/FMATS.2018.00042/BIBTEX.

[27] F. Körmann, Y. Ikeda, B. Grabowski, M.H.F. Sluiter, Phonon broadening in high entropy alloys, NPJ Comput Mater 3 (2017). https://doi.org/10.1038/s41524-017-0037-8.

[28] M. Caro, L.K. Béland, G.D. Samolyuk, R.E. Stoller, A. Caro, Lattice thermal conductivity of multi-component alloys, J Alloys Compd 648 (2015) 408–413. https://doi.org/10.1016/j.jallcom.2015.06.035.

[29] L.K. Béland, C. Lu, Y.N. Osetskiy, G.D. Samolyuk, A. Caro, L. Wang, R.E. Stoller, Features of primary damage by high energy displacement cascades in concentrated Ni-based alloys, J Appl Phys 119 (2016) 85901. https://doi.org/10.1063/1.4942533.

[30] Y. Zhang, Y.N. Osetsky, W.J. Weber, Tunable Chemical Disorder in Concentrated Alloys: Defect Physics and Radiation Performance, Chem Rev 122 (2022) 789–829. https://doi.org/10.1021/ACS.CHEMREV.1C00387/ASSET/IMAGES/LARGE/CR1C00387_0027.JPEG.

[31] G.S. Was, Fundamentals of radiation materials science: Metals and alloys, second edition, Fundamentals of Radiation Materials Science: Metals and Alloys, Second Edition (2016) 1–1002. https://doi.org/10.1007/978-1-4939-3438-6.

[32] C. Parkin, W.-Y. Chen, M. Li, K. Sridharan, A. Couet, Microstructural evolution of compositionally complex solid-solution alloys under in-situ dual-beam irradiation, Journal of Nuclear Materials 589 (2024) 154827. https://doi.org/10.1016/J.JNUCMAT.2023.154827.

[33] K. Jin, C. Lu, L.M. Wang, J. Qu, W.J. Weber, Y. Zhang, H. Bei, Effects of compositional complexity on the ion-irradiation induced swelling and hardening in Ni-containing equiatomic alloys, Scr Mater 119 (2016) 65–70. https://doi.org/10.1016/J.SCRIPTAMAT.2016.03.030.

[34] A. Kamboj, N. Perry, E.A. Marquis, Microstructure evolution in Cr0.6FeNiMn and CrFeNiCoPd under ion irradiation, Journal of Nuclear Materials 589 (2024) 154837. https://doi.org/10.1016/J.JNUCMAT.2023.154837.

[35] C. Li, X. Hu, T. Yang, N. Kiran Kumar, B.D. Wirth, S.J. Zinkle, Neutron irradiation response of a Co-free high entropy alloy, (2019). https://www.elsevier.com/open-access/userlicense/1.0/ (accessed December 17, 2023).

[36] H. Wen, Enhancing irradiation tolerance of steels via nanostructuring by innovative manufacturing techniques, (n.d.).

[37] J. W. Nielsen, Verification and Validation Testing of MCNP and ORIGEN2 Computer Codes for Idaho National Laboratory (INL High Performance Computing (HPC) Systems, TEV-2944 Revision 4 (2019).

[38] C.M. Parish, K.G. Field, A.G. Certain, J.P. Wharry, Application of STEM characterization for investigating radiation effects in BCC Fe-based alloys, J Mater Res 30 (2015) 1275–1289. https://doi.org/10.1557/JMR.2015.32.

[39] D.J. Edwards, E.P. Simonen, F.A. Garner, L.R. Greenwood, B.M. Oliver, S.M. Bruemmer, Influence of irradiation temperature and dose gradients on the microstructural evolution in neutron-irradiated 316SS, Journal of Nuclear Materials 317 (2003) 32–45. https://doi.org/10.1016/S0022-3115(03)00003-5.

[40] B.H. Sencer, G.S. Was, M. Sagisaka, Y. Isobe, G.M. Bond, F.A. Garner, Proton irradiation emulation of PWR neutron damage microstructures in solution annealed 304 and cold-worked 316 stainless steels, Journal of Nuclear Materials 323 (2003) 18–28. https://doi.org/10.1016/J.JNUCMAT.2003.07.007.

[41] X. Zhong, C.A. Wade, P.J. Withers, X. Zhou, C. Cai, S.J. Haigh, M.G. Burke, Comparing Xe+pFIB and Ga+FIB for TEM sample preparation of Al alloys: Minimising FIB-induced artefacts, J Microsc 282 (2021) 101. https://doi.org/10.1111/JMI.12983.

[42] J.M. Cowley, ] M Cowleyt, X-Ray Measurement of Order in Single Crystals of Cu3Au, J Appl Phys 21 (1950) 24–30. https://doi.org/10.1063/1.1699415.

[43] E. Antillon, C. Woodward, S.I. Rao, B. Akdim, T.A. Parthasarathy, Chemical short range order strengthening in a model FCC high entropy alloy, Acta Mater 190 (2020) 29–42. https://doi.org/10.1016/J.ACTAMAT.2020.02.041.

[44] Y. Wu, F. Zhang, X. Yuan, H. Huang, X. Wen, Y. Wang, M. Zhang, H. Wu, X. Liu, H. Wang, S. Jiang, Z. Lu, Short-range ordering and its effects on mechanical properties of high-entropy alloys, J Mater Sci Technol 62 (2021) 214–220. https://doi.org/10.1016/J.JMST.2020.06.018.

[45] Q.J. Li, H. Sheng, E. Ma, Strengthening in multi-principal element alloys with local-chemical-order roughened dislocation pathways, Nature Communications 2019 10:1 10 (2019) 1–11. https://doi.org/10.1038/s41467-019-11464-7.

[46] R. Zhang, S. Zhao, J. Ding, Y. Chong, T. Jia, C. Ophus, M. Asta, R.O. Ritchie, A.M. Minor, Short-range order and its impact on the CrCoNi medium-entropy alloy, Nature 2020 581:7808 581 (2020) 283–287. https://doi.org/10.1038/s41586-020-2275-z.

[47] Z. Zhang, Z. Su, B. Zhang, Q. Yu, J. Ding, T. Shi, C. Lu, R.O. Ritchie, E. Ma, Effect of local chemical order on the irradiation-induced defect evolution in CrCoNi medium-entropy alloy, Proc Natl Acad Sci U S A 120 (2023) e2218673120. https://doi.org/10.1073/PNAS.2218673120/SUPPL_FILE/PNAS.2218673120.SAPP.PDF.

[48] C. Lu, L. Niu, N. Chen, K. Jin, T. Yang, P. Xiu, Y. Zhang, F. Gao, H. Bei, S. Shi, M.R. He, I.M. Robertson, W.J. Weber, L. Wang, Enhancing radiation tolerance by controlling defect mobility and migration pathways in multicomponent single-phase alloys, Nature Communications 2016 7:1 7 (2016) 1–8. https://doi.org/10.1038/ncomms13564.

[49] B. Xing, X. Wang, W.J. Bowman, P. Cao, Short-range order localizing diffusion in multi-principal element alloys, Scr Mater 210 (2022) 114450. https://doi.org/10.1016/J.SCRIPTAMAT.2021.114450.

[50] S. Zhao, Role of chemical disorder and local ordering on defect evolution in high-entropy alloys, Phys Rev Mater 5 (2021) 103604. https://doi.org/10.1103/PHYSREVMATERIALS.5.103604/FIGURES/11/MEDIUM.

[51] Y. Wu, F. Zhang, X. Yuan, H. Huang, X. Wen, Y. Wang, M. Zhang, H. Wu, X. Liu, H. Wang, S. Jiang, Z. Lu, Short-range ordering and its effects on mechanical properties of high-entropy alloys, J Mater Sci Technol 62 (2021) 214–220. https://doi.org/10.1016/J.JMST.2020.06.018.

[52] P. Cao, How Does Short-Range Order Impact Defect Kinetics in Irradiated Multiprincipal Element Alloys?, Acc Mater Res 2 (2021) 71–74. https://doi.org/10.1021/ACCOUNTSMR.0C00102/ASSET/IMAGES/LARGE/MR0C00102_0003.JPEG.

[53] D. Chen, K. Murakami, K. Dohi, K. Nishida, Z. Li, N. Sekimura, The effects of loop size on the unfaulting of Frank loops in heavy ion irradiation, Journal of Nuclear Materials 529 (2020) 151942. https://doi.org/10.1016/J.JNUCMAT.2019.151942.

[54] S. M. , B.S. Dash, D. Ramachandran, P. C. , K. V. , Defects analysis in low displacement damage neutron-irradiated austenitic stainless steels, Journal of Nuclear Materials 599 (2024) 155234. https://doi.org/10.1016/J.JNUCMAT.2024.155234.

[55] D.T. Pierce, J.A. Jiménez, J. Bentley, D. Raabe, C. Oskay, J.E. Wittig, The influence of manganese content on the stacking fault and austenite/ε-martensite interfacial energies in Fe–Mn–(Al–Si) steels investigated by experiment and theory, Acta Mater 68 (2014) 238–253. https://doi.org/10.1016/J.ACTAMAT.2014.01.001.

[56] S.J. Zinkle, L.E. Seitzman, W.G. Wolfer, S.J. Zinkle, W.G. Wolfer, I. Energy calculations for pure metals, Philosophical Magazine A 55 (1987) 111–125. https://doi.org/10.1080/01418618708209803.

[57] A. Daramola, A. Fraczkiewicz, G. Bonny, G. Adjanor, G. Monnet, C. Domain, Physical insight into interactions of interstitial loops and dislocation lines in austenitic high entropy alloys: atomic-scale modelling, Journal of Nuclear Materials 592 (2024) 154959. https://doi.org/10.1016/J.JNUCMAT.2024.154959.

[58] D. Rodney, Molecular dynamics simulation of screw dislocations interacting with interstitial frank loops in a model FCC crystal, Acta Mater 52 (2004) 607–614. https://doi.org/10.1016/J.ACTAMAT.2003.09.044.

[59] S. Hayakawa, Y. Hayashi, T. Okita, M. Itakura, K. Suzuki, Y. Kuriyama, Effects of stacking fault energies on the interaction between an edge dislocation and an 8.0-nm-diameter Frank loop of self-interstitial atoms, Nuclear Materials and Energy 9 (2016) 581–586. https://doi.org/10.1016/J.NME.2016.10.010.

[60] T. Kadoyoshi, H. Kaburaki, F. Shimizu, H. Kimizuka, S. Jitsukawa, J. Li, Molecular dynamics study on the formation of stacking fault tetrahedra and unfaulting of Frank loops in fcc metals, Acta Mater 55 (2007) 3073–3080. https://doi.org/10.1016/J.ACTAMAT.2007.01.010.

[61] A. Kamboj, E.A. Marquis, Effect of dose rate on the phase stability of a CrFeNiMn alloy, Scr Mater 215 (2022) 114697. https://doi.org/10.1016/J.SCRIPTAMAT.2022.114697.

[62] K. Adachi, C.M. Wayman, Transformation behavior of nearly stoichiometric Ni-Mn alloys, Metallurgical Transactions A 16 (1985) 1567–1579. https://doi.org/10.1007/BF02663013.

[63] L. Ding, P.F. Ladwig, X. Yan, Y.A. Chang, Thermodynamic stability and diffusivity of near-equiatomic Ni-Mn alloys, Appl Phys Lett 80 (2002) 1186–1188. https://doi.org/10.1063/1.1450042.

[64] F. Bergner, C. Pareige, M. Hernández-Mayoral, L. Malerba, C. Heintze, Application of a three-feature dispersed-barrier hardening model to neutron-irradiated Fe–Cr model alloys, Journal of Nuclear Materials 448 (2014) 96–102. https://doi.org/10.1016/J.JNUCMAT.2014.01.024.

[65] P.D. Edmondson, S.A. Briggs, Y. Yamamoto, R.H. Howard, K. Sridharan, K.A. Terrani, K.G. Field, Irradiation-enhanced α′ precipitation in model FeCrAl alloys, Scr Mater 116 (2016) 112–116. https://doi.org/10.1016/J.SCRIPTAMAT.2016.02.002.

[66] K.G. Field, K.C. Littrell, S.A. Briggs, Precipitation of α′ in neutron irradiated commercial FeCrAl alloys, Scr Mater 142 (2018) 41–45. https://doi.org/10.1016/J.SCRIPTAMAT.2017.08.022.

[67] L. Zhang, Z. Hu, L. Zhang, H. Wang, J. Li, Z. Li, J. Yu, B. Wu, Enhancing the strength-ductility trade-off in a NiCoCr-based medium-entropy alloy with the synergetic effect of ultra fine precipitates, stacking faults, dislocation locks and twins, Scr Mater 211 (2022) 114497. https://doi.org/10.1016/J.SCRIPTAMAT.2021.114497.

[68] Q. Zhang, P.K. Liaw, H.J. Yang, J.W. Qiao, Short-range-ordering strengthening and the evolution of dislocation-nucleation modes in an Fe40Mn20Cr20Ni20 high-entropy alloy, Materials Science and Engineering: A 873 (2023) 145038. https://doi.org/10.1016/J.MSEA.2023.145038.

[69] Z. Sun, C. Shi, C. Liu, H. Shi, J. Zhou, The effect of short-range order on mechanical properties of high entropy alloy Al0.3CoCrFeNi, Mater Des 223 (2022) 111214. https://doi.org/10.1016/J.MATDES.2022.111214.

[70] H. Arkoub, M. Jin, Impact of chemical short-range order on radiation damage in Fe-Ni-Cr alloys, Scr Mater 229 (2023) 115373. https://doi.org/10.1016/J.SCRIPTAMAT.2023.115373.

[71] Q. Ding, X. Fu, D. Chen, H. Bei, B. Gludovatz, J. Li, Z. Zhang, E.P. George, Q. Yu, T. Zhu, R.O. Ritchie, Real-time nanoscale observation of deformation mechanisms in CrCoNi-based medium- to high-entropy alloys at cryogenic temperatures, Materials Today 25 (2019) 21–27. https://doi.org/10.1016/J.MATTOD.2019.03.001.

[72] S. Moniri, Y. Yang, J. Ding, Y. Yuan, J. Zhou, L. Yang, F. Zhu, Y. Liao, Y. Yao, L. Hu, P. Ercius, J. Miao, Three-dimensional atomic structure and local chemical order of medium- and high-entropy nanoalloys, Nature 2023 624:7992 624 (2023) 564–569. https://doi.org/10.1038/s41586-023-06785-z.